

## Experimentally validated broadband self-collimation of elastic waves

Soo-Ho Jo<sup>a,1</sup>, Yiwei Xia<sup>b,1</sup>, Adriane G. Moura<sup>b</sup>, Heonjun Yoon<sup>c,\*</sup>, Yong Chang Shin<sup>a</sup>, Alper Erturk<sup>b</sup>, Byeng D. Youn<sup>a,d,e</sup>

<sup>a</sup> Department of Mechanical and Aerospace Engineering, Seoul National University, Seoul 08826, Republic of Korea

<sup>b</sup> The George W. Woodruff School of Mechanical Engineering, Georgia Institute of Technology, Atlanta, GA 30332, United States

<sup>c</sup> School of Mechanical Engineering, Soongsil University, Seoul 06978, Republic of Korea

<sup>d</sup> Institute of Advanced Machines and Design, Seoul National University, Seoul 08826, Republic of Korea

<sup>e</sup> OnePredict Inc., Seoul 08826, Republic of Korea



### ARTICLE INFO

#### Keywords:

Self-collimation  
Equi-frequency contour  
Phononic crystal  
Anisotropy  
Broadband

### ABSTRACT

One extraordinary phenomenon exhibited by phononic crystals (PnCs) is that they can manipulate oblique incident waves in a target direction via proper refraction, commonly called wave self-collimation. Although prior studies have demonstrated self-collimation of electromagnetic and acoustic waves, only a few studies have examined elastic waves in this context. If a PnC is designed to represent rectangular-like and/or parallel-line-like equi-frequency contour (EFCs), elastic waves can be self-collimated in either horizontal or vertical directions. However, in the existing literature, there is no theoretical rationale for realizing rectangular-like and/or parallel-line-like EFCs; besides, broadband self-collimation of elastic waves has not yet been explored. Therefore, we propose to derive the material property requirement for an anisotropic PnC to exhibit rectangular-like EFCs (a range of low frequencies) and parallel-line-like EFCs (a range of high frequencies) in the case of elastic waves. Furthermore, by inherently adjoining two frequency ranges of the rectangular-like and parallel-line-like EFCs at a certain frequency, broadband self-collimation covering the entire range of frequencies can be achieved. With the designed anisotropic PnC that fulfills the proposed material property requirement, self-collimation for  $S_0$  Lamb waves is numerically simulated and experimentally demonstrated over a broad range of frequencies.

### 1. Introduction

A phononic crystal (PnC) is an engineered structure that consists of periodically arranged unit cells to exhibit properties beyond what is available in ordinary materials [1–10]. One extraordinary phenomenon of PnCs is their ability to manipulate any oblique incident waves in a target direction, so-called wave self-collimation [11–15]. One principle of self-collimation is to control the directions of energy transport in an equi-frequency contour (EFC). An EFC is a constant-frequency contour of three-dimensional dispersion curves, as shown in Fig. 1 (a), which can quantify the directions of both wave vectors and the polarization vectors within a medium [16,17]. In Fig. 1 (b), the vector  $\mathbf{k}_w$  from the origin to the EFC represents the direction along which the wavefront is propagated, and the normal vector  $\mathbf{k}_e$  of the EFC represents the direction along which wave energy is transported [18]. If a PnC is designed to exhibit rectangular-like or parallel-line-like EFCs, wave energy will be transported in either horizontal or vertical directions, thus enabling self-collimation.

In the case of electromagnetic waves, Chigrin et al. [19] presented self-collimated light beams at narrowband frequencies near a band gap.

Prather et al. [20] organized several potential engineering applications of self-collimation, including a channel-less waveguide, a tunable splitter, an optical switch, and an all-optical analog-to-digital converter. Li et al. [21] proposed a gyromagnetic unit cell to achieve one-way self-collimation. For acoustic waves, Li et al. [22] and Wen et al. [23] examined acoustic beam splitting and acoustic directional radiation using self-collimation, respectively. Shi et al. [24] doubled the frequency bandwidth of acoustic self-collimation using a sequential series of PnCs with the same period but a different filling fraction. However, only a few studies have been presented for the case of elastic waves; this is due to a complex tensor form of their governing equation. Liu et al. [25] investigated self-collimation under transverse elastic waves. Park et al. [26] executed topology optimization of a PnC for flattening the curvature of a rectangular-like EFC at a certain frequency. Cheng et al. [27] proposed a new design of a PnC composed of auxetic star-shaped honeycomb structures for self-collimation.

With respect to self-collimation of elastic waves in a PnC, two questions of importance can be posed: (1) how can a PnC be designed to have rectangular-like and/or parallel-line-like EFCs? and (2) how can elastic waves be self-collimated at broadband frequencies? To answer these questions, we newly propose material property requirement for

\* Corresponding author.

E-mail address: [heonjun@ssu.ac.kr](mailto:heonjun@ssu.ac.kr) (H. Yoon).

<sup>1</sup> Soo-Ho Jo and Yiwei Xia contributed equally to this work as the first author.

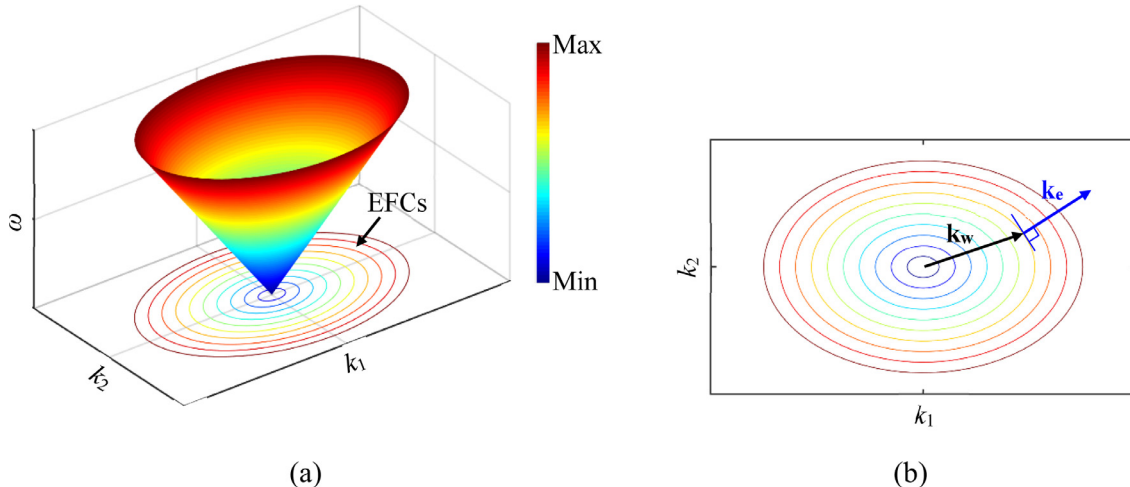


**Fig. 1.** Concept of EFCs for a nondispersive wave mode: (a) constant-frequency contours in three-dimensional dispersion curves; (b) wavefront vector  $\mathbf{k}_w$  and energy transport vector  $\mathbf{k}_e$ .

an anisotropic PnC to exhibit broadband self-collimation in the case of longitudinal elastic waves (e.g.,  $S_0$  Lamb waves in a thin plate case). There have been several efforts on elastic wave propagation in PnCs with asymmetric lattices that possess anisotropic properties [28–32]. Our primary interest is to fundamentally examine effective material properties required for achieving self-collimation in EFC analysis and to thoroughly investigate the broadband self-collimation capabilities of the designed anisotropic PnC that satisfies the proposed material property requirement. Finally, self-collimation for  $S_0$  Lamb waves is experimentally demonstrated at broadband frequencies. This study provides insightful theoretical rationale for anisotropic PnCs to realize the broadband self-collimation for elastic waves.

The rest of this paper is organized into the following sections. Section 2 describes the material property requirement for self-collimation of  $S_0$  Lamb waves. Section 3 presents EFC analysis of the anisotropic PnC that satisfies the proposed material property requirement. Numerical simulations and experiments examining self-collimation performance of the anisotropic PnC are demonstrated at broadband frequencies in Section 4. Finally, the conclusions of this work are provided in Section 5.

## 2. Proposed material property requirement for self-collimation of $S_0$ Lamb waves

If the lattice constant of a unit cell is much smaller than the wavelength of the elastic waves propagating through a host plate, a PnC equivalently behaves as an effective medium (a homogeneous solid) [33,34]. In this work, a term 'effective' has the same meaning with a term 'homogenized'. Under the assumption of plane harmonic wave motions at an angular frequency  $\omega$ , the governing equation for elastic waves in a homogeneous solid, the so-called Christoffel equation [18], is as follows:

$$C_{ijkl}^{\text{eff}} k_j k_l V_i = \rho^{\text{eff}} \omega^2 V_i \quad (1)$$

where  $k_i$  and  $V_i$  denote a component of a wave vector  $\mathbf{k}$  and a particle velocity vector  $\mathbf{V}$  in the  $i$ -th direction, respectively;  $\rho^{\text{eff}}$  and  $C_{ijkl}^{\text{eff}}$  are the density and the fourth-order tensor of elastic constants of the effective medium, respectively. Here, the  $6 \times 6$  second-order tensor form of the elastic constants, written in Voigt notation, would be used instead [35]. When the effective medium is symmetric with respect to its principal axes ( $x_1$ - and  $x_2$ -axes in this study), the longitudinal-transverse mode coupling constants of  $C_{16}^{\text{eff}}$  and  $C_{26}^{\text{eff}}$  will be zero [16,36]. For a thin plate with plane stress conditions, Christoffel equation can be rewritten as

follows:

$$\left( \begin{bmatrix} C_{11}^{\text{eff}} k_1^2 + C_{66}^{\text{eff}} k_2^2 & (C_{12}^{\text{eff}} + C_{66}^{\text{eff}}) k_1 k_2 \\ (C_{12}^{\text{eff}} + C_{66}^{\text{eff}}) k_1 k_2 & C_{66}^{\text{eff}} k_1^2 + C_{22}^{\text{eff}} k_2^2 \end{bmatrix} - \begin{bmatrix} \rho^{\text{eff}} \omega^2 & 0 \\ 0 & \rho^{\text{eff}} \omega^2 \end{bmatrix} \right) \begin{bmatrix} V_1 \\ V_2 \end{bmatrix} = \begin{bmatrix} 0 \\ 0 \end{bmatrix} \quad (2)$$

In terms of  $|\mathbf{k}|$ ,  $\cos\theta$ , and  $\sin\theta$ , Eq. (2) can be rewritten as follow:

$$\left( \begin{bmatrix} C_{11}^{\text{eff}} \cos^2 \theta + C_{66}^{\text{eff}} \sin^2 \theta & (C_{12}^{\text{eff}} + C_{66}^{\text{eff}}) \cos \theta \sin \theta \\ (C_{12}^{\text{eff}} + C_{66}^{\text{eff}}) \cos \theta \sin \theta & C_{66}^{\text{eff}} \cos^2 \theta + C_{22}^{\text{eff}} \sin^2 \theta \end{bmatrix} - \begin{bmatrix} \rho^{\text{eff}} \omega^2 & 0 \\ 0 & \rho^{\text{eff}} \omega^2 \end{bmatrix} \right) \begin{bmatrix} V_1 \\ V_2 \end{bmatrix} = \begin{bmatrix} 0 \\ 0 \end{bmatrix} \quad (3)$$

where  $|\mathbf{k}|$  is the magnitude of the wave vector  $\mathbf{k}$ , calculated by  $(k_1^2 + k_2^2)^{1/2}$ ;  $k_1$  and  $k_2$  can be expressed as  $|\mathbf{k}| \cos\theta$  and  $|\mathbf{k}| \sin\theta$ , respectively. Once both effective elastic moduli and the angular frequency  $\omega$  are determined, the zero determinant in Eq. (3) provides two solutions of  $|\mathbf{k}|$  for a certain  $\theta$  that ranges from zero to  $2\pi$ . Each of the solutions corresponds to  $S_0$  and  $A_0$  Lamb wave modes for a thin plate case, respectively. Then,  $k_1$  and  $k_2$  can be obtained for the given  $\theta$ . Finally, a EFC can be defined as a function of  $k_1$  and  $k_2$ , as shown in Fig. 1. In general, an isotropic material exhibits a purely circular EFC.

If the elastic constants of  $C_{11}^{\text{eff}}$ ,  $C_{22}^{\text{eff}}$ ,  $C_{12}^{\text{eff}}$ , and  $C_{66}^{\text{eff}}$  satisfy the following relationship:

$$C_{11}^{\text{eff}} > C_{22}^{\text{eff}} \gg C_{12}^{\text{eff}}, C_{66}^{\text{eff}} \quad (4)$$

solutions of the zero determinant in Eq. (3) can be approximately decomposed into two decoupled equations of standard ellipses centered at the origin; thereby, EFCs can be regarded as a superposition of two ellipses. Note that a major axis of one ellipse is parallel to the  $x_1$ -axis and that of the other is vertical to the  $x_1$ -axis. In both ellipses, polarized vectors at the wavefront follow  $S_0$  Lamb waves around the minor axis, while they follow  $A_0$  Lamb waves around the major axis. It is worth pointing out that the ellipses around the minor axis can be regarded as flat lines in a certain range of directions, due to their considerably small curvature. Since four flat lines near the two minor axes in each ellipse meet at the four angular points, a rectangular-like EFC can be obtained for  $S_0$  Lamb waves. As an example, Fig. 2 (a) shows a rectangular-like EFC (colored in blue) for  $S_0$  Lamb waves, that satisfies the material property requirement in Eq. (4). In particular, the four sides of the rectangular-like EFC tend to be more flattened as the ratio of  $C_{11}^{\text{eff}}$  and  $C_{22}^{\text{eff}}$  to  $C_{66}^{\text{eff}}$  and  $C_{12}^{\text{eff}}$  increases.

On the other hand, if the PnC, which satisfies the proposed material property requirement of  $C_{11}^{\text{eff}} > C_{22}^{\text{eff}}$ , exhibits a partial band gap in the  $x_2$ -axis, the upper and lower edges in its rectangular-like EFC would

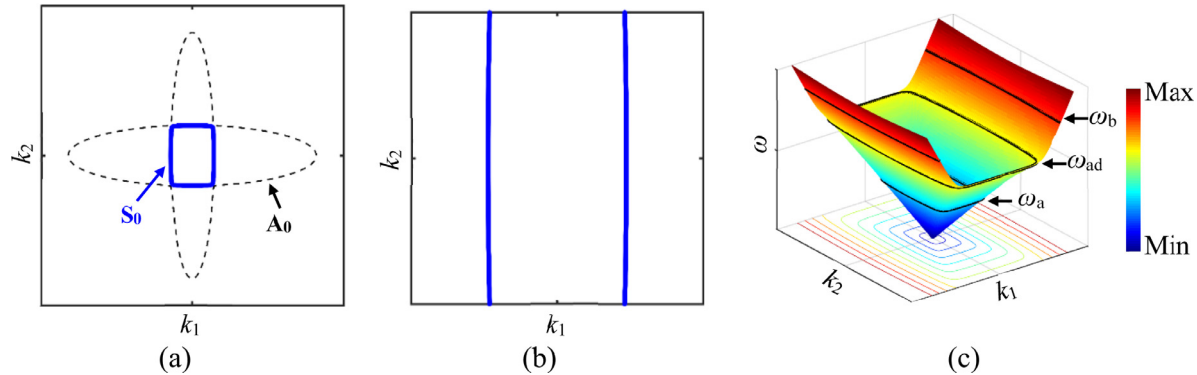


**Fig. 2.** The formation of (a) rectangular-like and (b) parallel-line-like EFCs for the case of  $S_0$  Lamb waves, when satisfying the proposed material property requirement; and (c) a scheme to achieve broadband self-collimation.

not be observed. This is because a partial band gap represents the non-real wave vectors [37,38]. A partial band gap refers to an extraordinary phenomenon where elastic waves cannot be propagated through PnCs in a certain incident direction [39,40]. From the viewpoint of EFCs, the partial band gap can be defined as a frequency range in which the EFCs are not closed in a specific certain direction [41]. Therefore, a parallel-line-like EFC can be obtained in the  $x_1$ -axis, as shown in Fig. 2 (b).

When a PnC is designed to satisfy the proposed material property requirement in Eq. (4), it can be seen in Fig. 2 (c) that the rectangular-like EFCs would be observed over a closed interval of low frequencies ( $\omega_a \leq \omega \leq \omega_{ad}$ ). As the frequency increases, both the length and width of the rectangular-like EFCs increase with the wavenumber. If the upper and lower edges of the rectangular-like EFCs meet the borders of the first Brillouin zone at the certain frequency  $\omega_{ad}$ , the rectangular-like EFCs are transformed into the parallel-line-like EFCs over a half-open interval of high frequencies ( $\omega_{ad} < \omega \leq \omega_b$ ). With the proposed material property requirement, the frequency ranges of rectangular-like and parallel-line-like EFCs are thus inherently adjoined at the frequency  $\omega_{ad}$  as shown in Fig. 2 (c). Finally, broadband self-collimation covering the entire ranges ( $\omega_a \leq \omega \leq \omega_b$ ) can be achieved for  $S_0$  Lamb waves by adjoining these two kinds of EFCs at  $\omega_{ad}$ . If one wants to realize broadband self-collimation by exploiting only the rectangular-like EFCs, the lattice constant of the unit cell needs to be much smaller to broaden the frequency range of the rectangular-like EFCs. However, due to the manufacturability of the PnC, it is impractical to make the unit cell extremely small. Therefore, the idea of adjoining frequency ranges of the rectangular-like and parallel-line-like EFCs enables to achieve broadband self-collimation with a macro-scale unit cell.

### 3. EFC analysis for the anisotropic PnC satisfying the proposed material property requirement

#### 3.1. Design and effective material properties for the anisotropic PnC

The unit cell under consideration, shown in Fig. 3 (a), is composed of an aluminum square lattice with a rectangular hole at its center. Design variables of the unit cell include: the lattice constant  $d$ , the thickness  $t$ , the width  $w$ , and the height  $h$  of the rectangular hole, respectively. Table 1 summarizes both the geometry of the unit cell and material properties of the aluminum.

It should be noted that the effective longitudinal elastic constants of  $C_{11}^{\text{eff}}$  and  $C_{22}^{\text{eff}}$  will be different, since the rectangular hole is not symmetric with respect to diagonal lines. This implies that the PnC will possess anisotropic effective material properties, even though the aluminum itself is an isotropic material.

Several research efforts have been made to characterize effective material properties of anisotropic PnCs [42–46]. Among them, static analysis can be performed since the unit cell has nothing to do with

**Table 1**  
Geometry of the unit cell and material properties of the aluminum.

Geometry	Lattice constant, $d$	9 mm
	Thickness, $t$	5 mm
	Width of the rectangular hole, $w$	8 mm
	Height of the rectangular hole, $h$	3 mm
Material properties (Aluminum)	Density, $\rho_{\text{al}}$	2700 kg/m <sup>3</sup>
	Young's modulus, $Y_{\text{al}}$	70 GPa
	Poisson's ratio, $\nu_{\text{al}}$	0.33

**Table 2**  
Effective material properties of the anisotropic PnC.

Effective material properties	Anisotropic PnC	
Density	$\rho^{\text{eff}}$	1900 kg/m <sup>3</sup>
Elastic constants	$C_{11}^{\text{eff}}$	47.5 GPa
	$C_{22}^{\text{eff}}$	12.6 GPa
	$C_{12}^{\text{eff}}$	2.38 GPa
	$C_{66}^{\text{eff}}$	1.54 GPa

any resonant structure and no impact on longitudinal-transverse mode coupling [16,36,47]. The effective density can be calculated by  $\rho_{\text{al}}(d^2 - wh)/d^2$ . Effective elastic constants can be calculated by the stress-strain relationship;  $C_{11}^{\text{eff}}$ ,  $C_{22}^{\text{eff}}$ , and  $C_{12}^{\text{eff}}$  govern the longitudinal deformations, while the remaining  $C_{66}^{\text{eff}}$  governs the transverse deformation.

A commercially available finite element analysis (FEA) software, COMSOL Multiphysics 5.4, was used for all analyses in numerical simulations. A loss factor of the structure is set as 0.0001 [48]. For a  $3 \times 3$  array of unit cells, Fig. 3 (b) and (c) show deforming behaviors of the array under tensile forces  $H$  and  $V$  in the  $x_1$ - and  $x_2$ -axes, respectively. Since the unit cell is periodically arranged in the  $x_1$ - and  $x_2$ -axes, respectively, periodic boundary conditions (PBCs) can be employed on interfaces among adjacent unit cells, according to Floquet-Bloch theorem [49,50]. Fig. 3 (d) shows deforming behaviors of the array under a shear force  $S$  in the  $x_1$ -axis, while PBCs are applied in the  $x_2$ -axis and zero displacements in the  $x_1$ -axis are employed at both left and right ends of the structure. Magnitudes of the tensile forces  $H$  and  $V$  and the shear force  $S$  are the same, denoted as  $F$ .

The elastic constants of  $C_{11}^{\text{eff}}$  and  $C_{22}^{\text{eff}}$  can be estimated from the Hooke's law  $F/(\delta_1 t)$  and  $F/(\delta_2 t)$ , where  $\delta_1$  and  $\delta_2$  are the average elongations in the  $x_1$ - and  $x_2$ -axes at load-acting surfaces in Fig. 3 (b) and (c), respectively. The elastic constant of  $C_{12}^{\text{eff}}$  can be estimated from  $C_{12}^{\text{eff}} F_{22}^{\text{PBC}}/F$  (or  $C_{22}^{\text{eff}} F_{11}^{\text{PBC}}/F$ ) in Fig. 3 (b) (or (c)) where  $F_{22}^{\text{PBC}}$  and  $F_{11}^{\text{PBC}}$  are average reaction forces outward normal directions at PBCs in Fig. 3 (b) and (c), respectively. Likewise, the elastic constant of  $C_{66}^{\text{eff}}$  can be estimated from  $2F/(u_2 t)$ , where  $u_2$  is an average displacement in the  $x_2$ -axis at load-acting surfaces.

Table 2 summarizes the estimated effective material properties of the anisotropic PnC. It can be seen that  $C_{11}^{\text{eff}}$  and  $C_{22}^{\text{eff}}$  are 19.9 times and

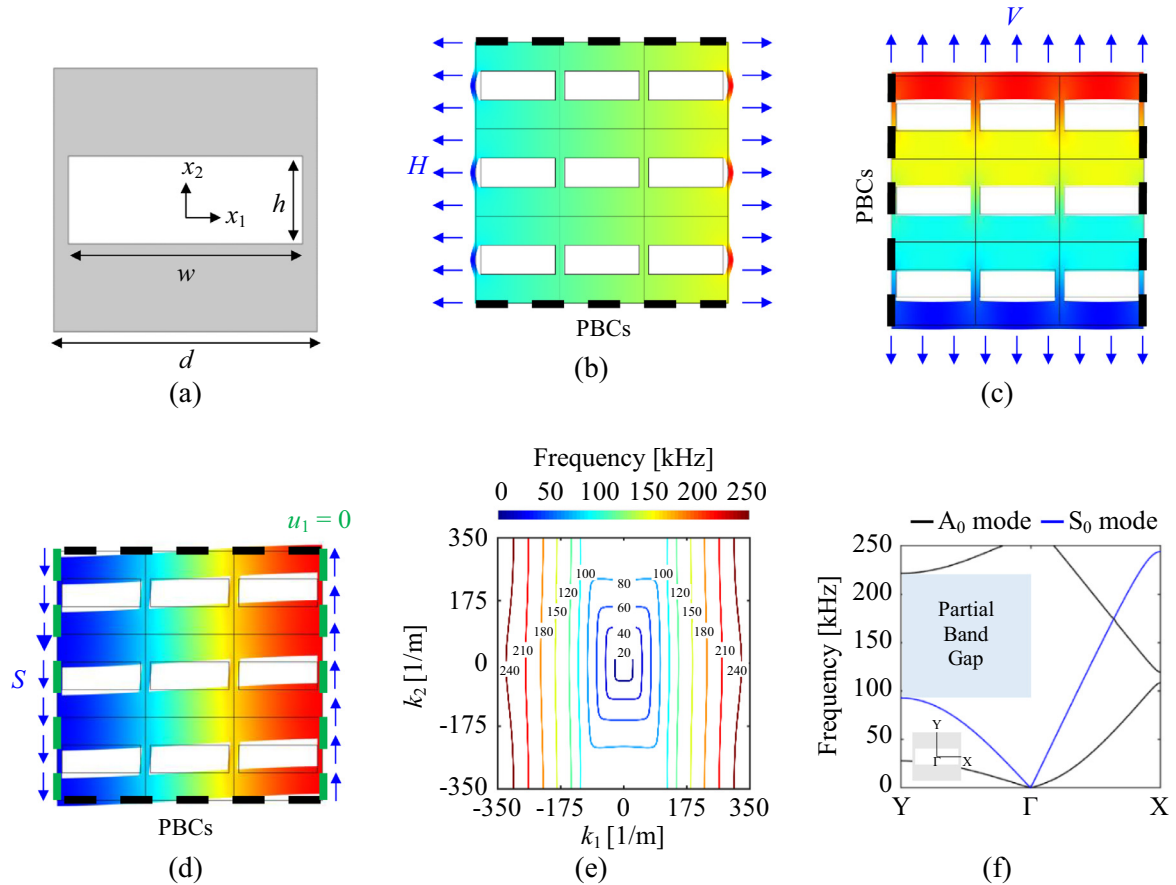


**Fig. 3.** Static analysis and EFC analysis for the unit cell: (a) a top view of the unit cell; static deforming behaviors under (b) a tensile force  $H$  in the  $x_1$ -axis ( $C_{11}^{\text{eff}}$  and  $C_{12}^{\text{eff}}$ ); (c) a tensile force  $V$  in the  $x_2$ -axis ( $C_{22}^{\text{eff}}$  and  $C_{12}^{\text{eff}}$ ); (d) a shear force  $S$  in the  $x_1$ -axis ( $C_{66}^{\text{eff}}$ ); (e) the formation of rectangular-like and parallel-line-like EFCs from 0 kHz to 220 kHz; and (f) the formation of the partial band gap from 93 kHz to 220 kHz in dispersion curves.

5.29 times larger than  $C_{12}^{\text{eff}}$ , respectively, while they are 30.8 times and 8.19 times larger than  $C_{66}^{\text{eff}}$ , respectively. It is known that the effective medium theory is generally based on the long-wavelength limit. However, since all effective material properties tend to gradually decrease together as the frequency increases [16], the Eq. (4) is still applicable at higher frequencies. Therefore, the anisotropic PnC can thus fulfill the proposed material property requirement over broadband frequencies, thereby enabling broadband self-collimation of elastic waves.

### 3.2. EFCs of the anisotropic PnC

By inserting the PBCs into the governing equation of the unit cell, an eigenvalue problem can be formulated as follows [51–53]:

$$([\mathbf{K}] + i\omega[\mathbf{C}] - \omega^2[\mathbf{M}])\{\mathbf{u}\} = \mathbf{0} \quad (5)$$

where  $[\mathbf{M}]$  and  $\{\mathbf{u}\}$  are the mass matrix and the displacement vector, respectively.  $[\mathbf{C}]$  and  $[\mathbf{K}]$  are the damping and the stiffness matrices, which are functions of the reciprocal wave vector  $\mathbf{k}(k_1, k_2)$ . At a certain angular frequency  $\omega$ , the EFC can be obtained by calculating a set of reciprocal wave vectors, which should be within a range from  $-\pi/d$  to  $\pi/d$ .

At frequencies ranging from 0 kHz to 250 kHz, Fig. 3 (e) presents the EFCs of  $S_0$  Lamb waves. In addition, for the purpose of investigating the formation of the partial band gap, Fig. 3 (f) depicts dispersion curves of the unit cell along some borderlines ( $Y \rightarrow \Gamma \rightarrow X$ ) of the first Brillouin zone [54], respectively; solid lines with blue and black indicate the band structures of  $S_0$  mode and  $A_0$  mode, respectively. It is found that the anisotropic PnC presents retangular-like EFCs at low broadband

frequencies, ranging from 0 kHz to 93 kHz, due to the proposed material property requirement. Further, since a partial band gap is created in the  $x_2$ -axis from 93 kHz to 220 kHz as shown in Fig. 3 (f), the upper and lower edges of the rectangular-like EFCs disappear. Therefore, the anisotropic PnC exhibits parallel-line-like EFCs at high broadband frequencies, ranging from 93 kHz to 220 kHz, due to the combined effects of the partial band gap in the  $x_2$ -axis and the proposed material property requirement. Here, it should be noted that whether  $S_0$  Lamb waves can be self-collimated along the  $x_1$ -axis depends on the incidence angle; a detailed explanation is provided in Appendix A.

The unit cell under consideration is a non-resonant type PnC. Unlike a resonant type metamaterial [30,55,56], which is designed for a certain target frequency, it is well known that a non-resonant type PnC is capable of exhibiting nearly constant effective material properties in a wide range of frequencies [36,46,57]. Therefore, the anisotropic PnC satisfies the material property requirement at broadband frequencies and is capable of obtaining rectangular-like and parallel-line-like EFCs at each wide range of frequencies. In addition, it is worth pointing out that inherently adjoining two ranges of frequencies near 93 kHz enables realization of broadband self-collimation for  $S_0$  Lamb waves from 0 kHz to 220 kHz.

## 4. Demonstration of broadband self-collimation of $S_0$ Lamb waves

### 4.1. Numerical simulation

Fig. 4 (a) shows a large aluminum plate with a  $25 \times 41$  array of unit cells deployed near the center of it; the width and the height of the anisotropic PnC domain are 225 mm and 369 mm, respectively. This study performed transient analysis to numerically investigate broadband

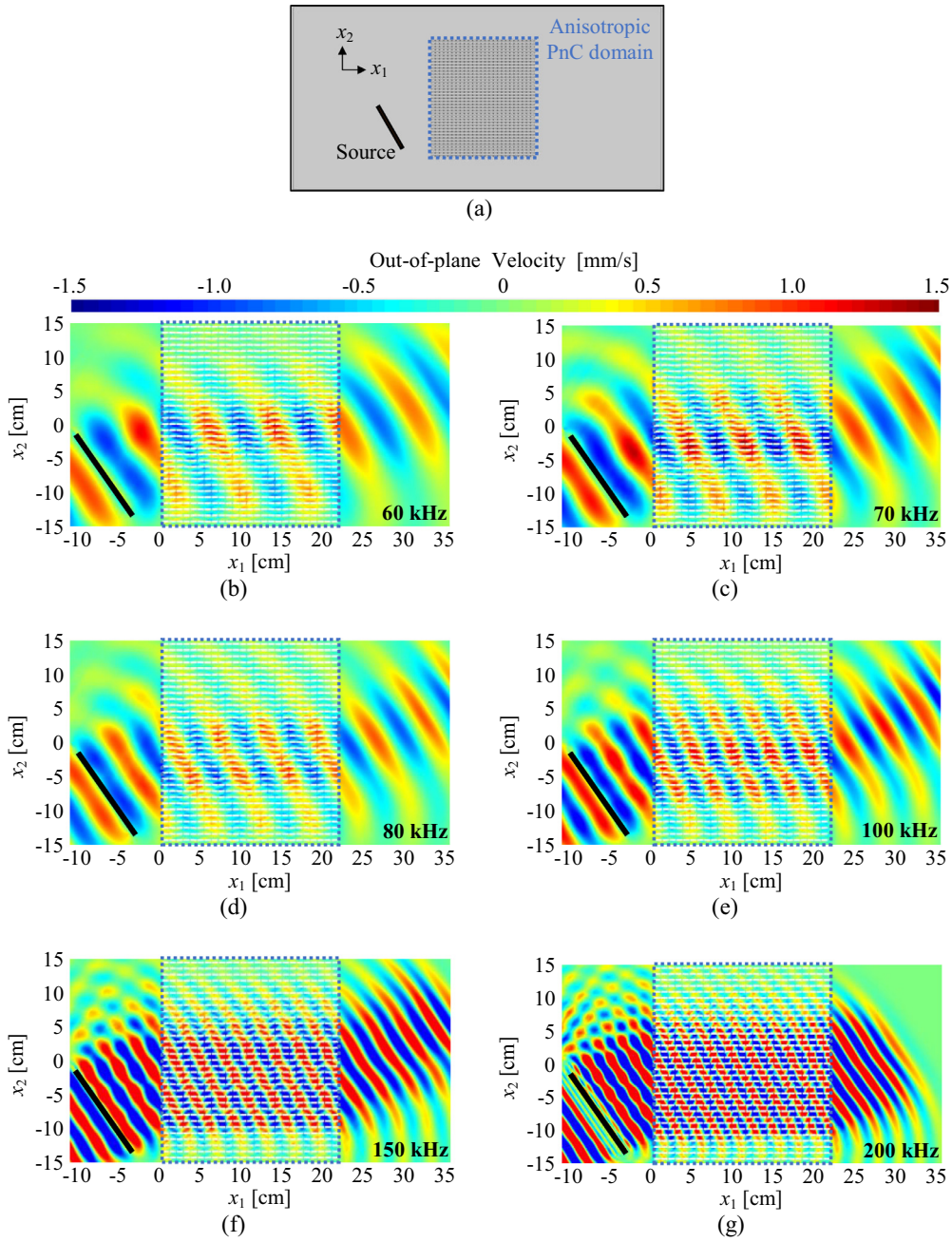


**Fig. 4.** FEA simulations for transient analysis: (a) system configuration; out-of-plane velocity fields of the structure at frequencies of (b) 60 kHz; (c) 70 kHz; (d) 80 kHz; (e) 100 kHz; (f) 150 kHz; and (g) 200 kHz.

self-collimation of \$S\_0\$ Lamb waves. To excite the oblique \$S\_0\$ Lamb waves into the anisotropic PnC domain, a line source is set to be inclined by \$150^\circ\$ with respect to the \$x\_1\$-axis. \$S\_0\$ Lamb waves are induced by exciting the line source by 16 cycles of sinusoidal bursts in the normal direction with a prescribed velocity of 10 mm/s, regardless of the exciting frequency.

To investigate whether \$S\_0\$ Lamb waves can be self-collimated at each frequency of rectangular-like and parallel-line-like EFCs, FEA simulation results are presented at six frequencies, including: 60, 70, and 80 kHz for the rectangular-like EFCs, and 100, 150, and 200 kHz for the parallel-line-like EFCs. Note that the anisotropic PnC can theoretically achieve self-collimation at arbitrary frequencies below 60 kHz; however, since the wavelength becomes longer as the frequency becomes lower, we

selected the frequency of 60 kHz as the lowest one for the rectangular-like EFCs, considering the manufacturable volume of the specimen and the transducer specifications in the experiments.

Figs. 4 (b) to (g) depict the calculated out-of-plane velocity fields at frequencies of 60, 70, 80, 100, 150, and 200 kHz, respectively. It can be seen in Figs. 4 (b) to (g) that \$S\_0\$ Lamb waves propagate only along the \$x\_1\$-axis inside the anisotropic PnC at all frequencies. Therefore, the capability of the anisotropic PnC for broadband self-collimation is confirmed through this FEA simulations. In addition, to validate the broadband self-collimation over a wide range of incidence angles, numerical simulation results for other incidence angles (i.e., \$20^\circ\$, \$40^\circ\$, and \$50^\circ\$) at frequencies of 60 kHz and 200 kHz are presented in Appendix B.

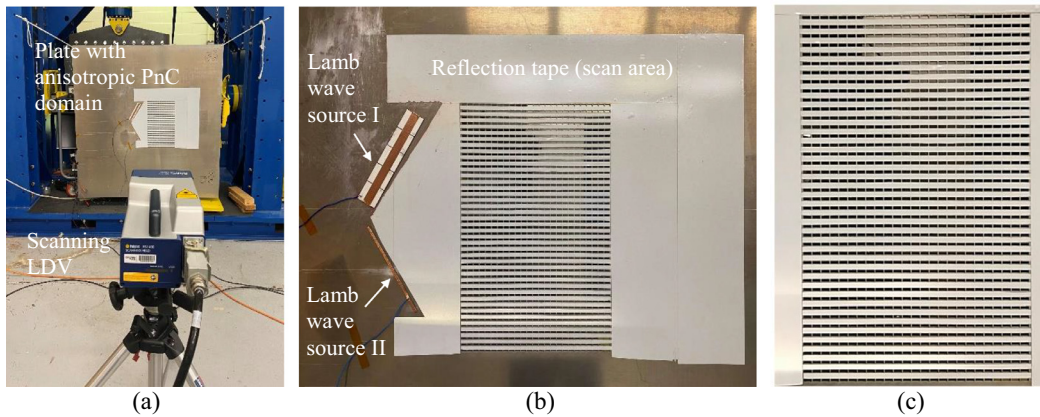


**Fig. 5.** Experimental setup showing the anisotropic PnC domain for self-collimation: (a) overall setup displaying the plate and scanning LDV; (b) close-up view showing the scan area as well as locations and orientations of piezoelectric line array sources for the  $S_0$  Lamb wave excitation; and (c) a view of the anisotropic PnC domain.

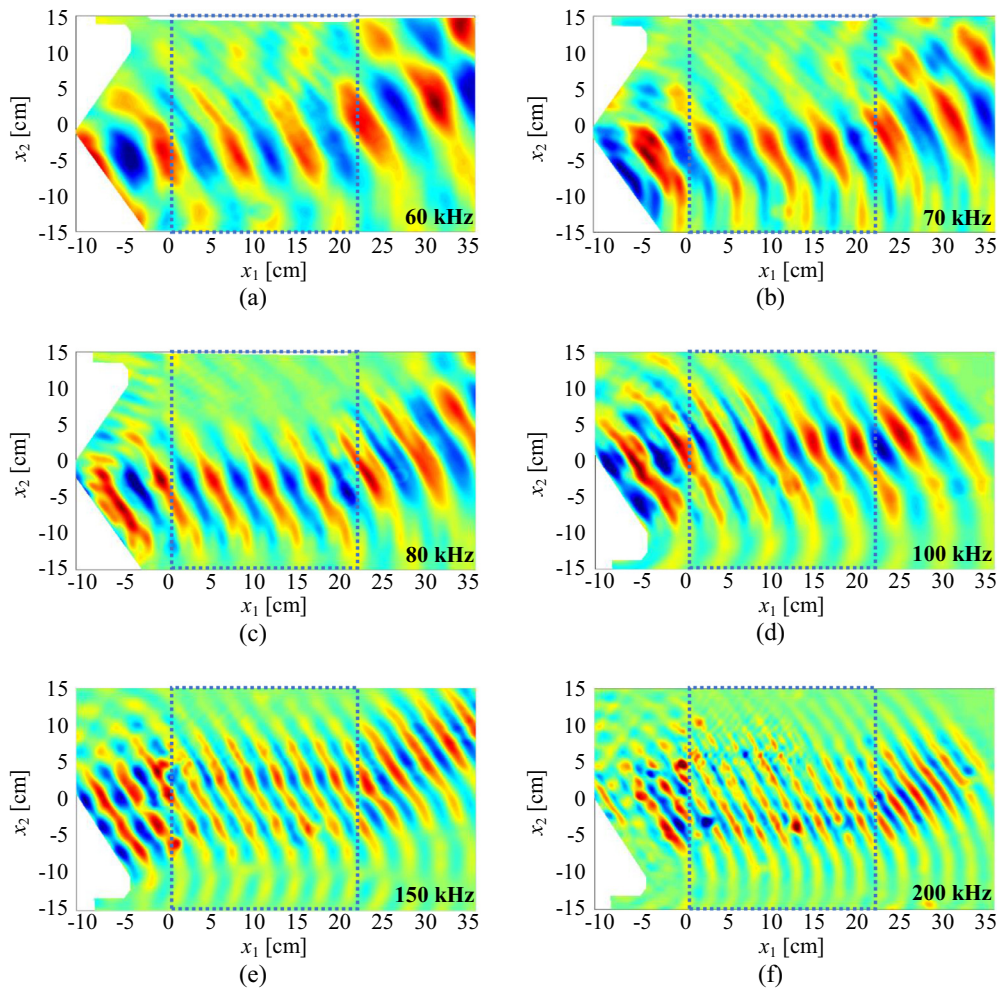


**Fig. 6.** Experimentally measured out-of-plane velocity fields at frequencies of (a) 60 kHz; (b) 70 kHz; (c) 80 kHz; (d) 100 kHz; (e) 150 kHz; and (f) 200 kHz (note that Figures (a) to (c) were obtained using Source I, while Figures (d) to (f) were obtained using Source II; for a convenient representation, Figures (a) to (c) are therefore flipped to plotting to be consistent with the orientation of numerical simulations).

When the incident  $S_0$  Lamb waves are fed into the anisotropic PnC, it could be partially reflected at the interfaces of the host aluminum plate and the anisotropic PnC due to the impedance mismatch. Therefore, the mechanical power of the transmitted wave in self-collimation would be less than that of the incident wave. The reflection coefficient of the velocity can be calculated by  $(Z_{\text{PnC}} - Z_{\text{al}})/(Z_{\text{PnC}} + Z_{\text{al}})$  where  $Z_{\text{al}}$  and  $Z_{\text{PnC}}$  in-

dicate the mechanical impedances of the aluminum and anisotropic PnC considering the incidence angle, respectively. Then, the reflection coefficient of the mechanical power is calculated by  $|Z_{\text{PnC}} - Z_{\text{al}}|^2 / |Z_{\text{PnC}} + Z_{\text{al}}|^2$  which is equal to the absolute square of the reflection coefficient of the velocity [58,59]. For a very low loss factor, the transmission coefficient of the mechanical power can be obtained from energy conservation. The

velocity amplitude of the reflected waves in the host aluminum plate is calculated as near 3 mm/s. As the velocity amplitude of the incident waves is 10 mm/s, the reflection and transmission coefficients of the mechanical power can be obtained as near 9% and 91%, respectively. In addition, it can be found that the wavefront is inclined by a certain angle with respect to the  $x_1$ -axis, even though the energy is transmitted in the  $x_1$ -axis. This can be described by Snell's law, which covers the refracted angle depending on the variation of wavenumbers (or phase velocities) of the host structure and anisotropic PnC at the interfaces. When the propagating waves on the host structure are fed into the anisotropic PnC, the  $x_2$ -directional wavenumber should be preserved at the interfaces; however, the  $x_1$ -directional wavenumber is changed, depending on the EFCs of the anisotropic PnC at a given frequency. The ratio of the  $x_2$ -directional wavenumber to the  $x_1$ -directional wavenumber can determine the inclined angle of the wavefront in the anisotropic PnC domain.

#### 4.2. Experimental validation

Experimental validation of the broadband self-collimation simulations was performed using the setup shown in Fig. 5 (a). This figure shows the fabricated plate with the attachment of piezoelectric line arrays for  $S_0$  Lamb wave excitation (Fig. 5 (b)) and a close-up view of the anisotropic PnC domain and machined unit cells (Fig. 5 (c)). To generate  $S_0$  Lamb waves at the desired frequencies, two line array sources were used (Source I for 60, 70, and 80 kHz and Source II for 100, 150, and 200 kHz), since the corresponding wavelength range is relatively wide. Source I (longer wavelength) includes five piezoelectric patches ( $30 \times 30 \times 1 \text{ mm}^3$ ) bonded as a line array ( $150 \times 30 \times 1 \text{ mm}^3$ ) to the aluminum plate on both sides at  $150^\circ$  relative to horizontal. For the shorter wavelength range, two piezoelectric patches ( $72.4 \times 5 \times 0.267 \text{ mm}^3$ ) were bonded as a line array ( $144.8 \times 5 \times 0.267 \text{ mm}^3$ ) to the aluminum plate on both sides at  $30^\circ$  relative to horizontal to form source II. The piezoelectric elements in the respective line arrays were connected in parallel and driven in phase (with each other as well as on both sides of the plate) to create  $S_0$  Lamb waves. Each source array was excited by 16 cycles of sinusoidal bursts at the desired frequencies (60, 70, 80 kHz with Source I and 100, 150, and 200 kHz with Source II) using a function generator (Agilent 33200A) and a voltage amplifier (Trek Model PZD350). A Polytec PSV-400 scanning laser Doppler vibrometer (LDV) was used to measure the resulting wave field by recording the out-of-plane velocity of the plate over a grid of points covering the domain of interest.

The overall out-of-plane velocity field was measured over a broad range of frequencies to explore the frequency dependence and to validate the numerical results. To confirm the performance over a range of frequencies, experiments were conducted for frequencies of 60, 70, 80, 100, 150, and 200 kHz. To filter the presence of  $A_0$  Lamb waves especially for long wavelength (lower frequency) cases, a two-dimensional circular averaging filter (pillbox) was applied, which is similar to a moving average filter in one-dimensional signals. The parameter radius was determined based on the ratio between the cutoff wavelength of  $S_0$  and  $A_0$  modes at each frequency and the scanning grid size. The process acted as a low-pass filter in the wavenumber domain so that  $S_0$  Lamb waves were kept while the  $A_0$  Lamb waves were filtered out. Therefore,  $S_0$  Lamb waves can be clearly observed in the time series response for all six frequencies, as shown in Fig. 6. For better comparison, the experimental results for 60, 70, and 80 kHz were flipped horizontally (due to the symmetric arrangement of the line arrays in Fig. 5 (b)) so that the source orientation is consistent with the simulation. It was found that  $S_0$  Lamb waves propagate only in the horizontal direction inside the anisotropic PnC at all frequencies. These experimental results agree very well with numerical simulations. It can be thus concluded from the experimental results that the anisotropic PnC is capable of self-collimation of  $S_0$  Lamb waves over a wide frequency range using the rectangular-like and parallel-line-like EFCs.

## 5. Conclusion

This study newly proposed the material property requirement for anisotropic phononic crystals (PnCs) to achieve broadband self-collimation of  $S_0$  Lamb waves. Theoretical framework is presented for obtaining rectangular-like and parallel-line-like equi-frequency contours (EFCs), along with numerical simulations and experimental validations of self-collimation over a range of frequencies. To the best of the authors' knowledge, no previous study has revealed such a relationship between the effective elastic moduli and EFCs, in terms of broadband self-collimation. It is noted that, if the effective elastic moduli of  $C_{11}^{\text{eff}}$  and  $C_{22}^{\text{eff}}$  are much larger than those of  $C_{12}^{\text{eff}}$  and  $C_{66}^{\text{eff}}$ , rectangular-like EFCs can be obtained. In such a case, if  $C_{11}^{\text{eff}}$  is larger than  $C_{22}^{\text{eff}}$ , a partial band gap can be formed in the  $x_2$ -axis, thereby enabling the realization of parallel-line-like EFCs in the  $x_1$ -axis. This study used an array of square lattices with rectangular holes, which possesses the required anisotropic material properties. With the help of non-resonant structure characteristics, the anisotropic PnC represented rectangular-like EFCs at low broadband frequencies and parallel-line-like EFCs at high broadband frequencies. By adjoining frequency ranges of the rectangular-like and parallel-line-like EFCs at a certain frequency, broadband self-collimation can be achieved for  $S_0$  Lamb waves. Lastly, results from both numerical simulations and experiments demonstrated that the anisotropic PnC satisfying the proposed material property requirement is capable of broadband self-collimation of  $S_0$  Lamb waves.

## Declaration of Competing Interest

The authors declare that they have no known competing financial interests or personal relationships that could have appeared to influence the work reported in this paper.

## CRediT authorship contribution statement

**Soo-Ho Jo:** Conceptualization, Methodology, Formal analysis, Writing - original draft, Writing - review & editing. **Yiwei Xia:** Investigation, Validation, Visualization, Writing - original draft, Writing - review & editing. **Adriane G. Moura:** Investigation, Validation, Visualization, Writing - original draft. **Heonjun Yoon:** Conceptualization, Formal analysis, Supervision, Project administration, Writing - original draft, Writing - review & editing. **Yong Chang Shin:** Conceptualization, Methodology, Formal analysis, Writing - review & editing. **Alper Erturk:** Investigation, Validation, Visualization, Writing - original draft, Writing - review & editing. **Byeng D. Youn:** Conceptualization, Funding acquisition, Writing - review & editing.

## Acknowledgments

This work was supported by the Basic Science Research Program through the National Research Foundation of Korea (NRF) funded by the Ministry of Education (2019R1A6A3A12032924).

## Appendix A. Effects of an incidence angle on self-collimation phenomenon

When an oblique incidence angle  $\theta_{\text{in}}$  is within an open interval ( $|\theta_{\text{in}}| < \theta_{\text{ag}}/2$ ) where the allowable angle  $\theta_{\text{ag}}$  is shown in Figs. A1 (a) and (b), the incident waves can be self-collimated in the  $x_1$ -axis over broadband frequencies. The allowable angle  $\theta_{\text{ag}}$  is defined as an angle formed by the intersection of diagonals in the rectangular-like EFCs, shown in Fig. A1 (a), or by the intersection of two lines crossing the endpoints of the parallel-line-like EFCs, shown in Fig. A1 (b). If the incidence angle is out of the open interval ( $|\theta_{\text{in}}| > \theta_{\text{ag}}/2$ ), the incident  $S_0$  Lamb waves would be self-collimated along the  $x_2$ -axis in a low frequency range exhibiting rectangular-like EFCs or totally reflected due to the partial band

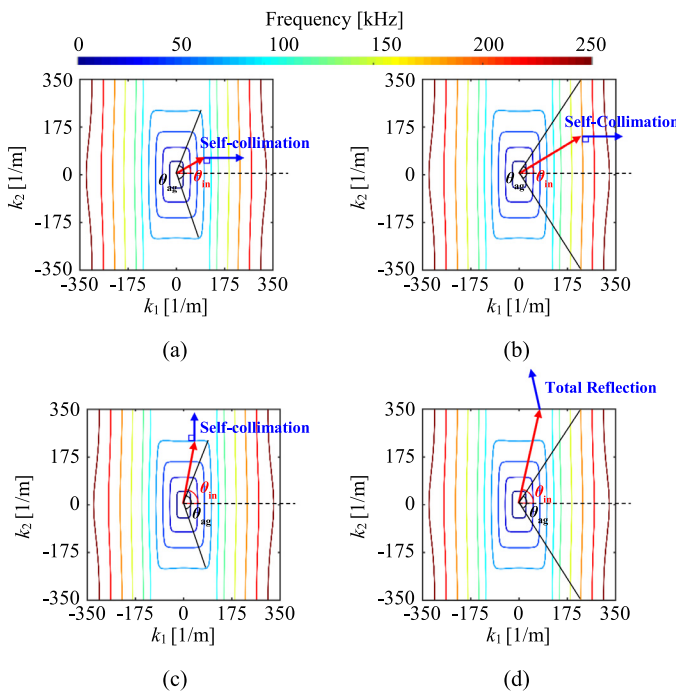


**Fig. A1.** Effects of an incidence angle  $\theta_{in}$  on self-collimation phenomenon:  $x_1$ -directional self-collimation for (a) rectangular-like and (b) parallel-line-like EFCs; (c)  $x_2$ -directional self-collimation for rectangular-like EFCs and (d) total reflection for parallel-line-like EFCs.

gap in a high frequency range exhibiting parallel-line-like EFCs, as depicted in Figs. A1 (c) and (d), respectively. Note that the allowable angle  $\theta_{ag}$  depends on the given frequency.

## Appendix B. Broadband self-collimation over a wide range of incidence angles

Fig. A2 depicts numerical simulation results for other incidence angles (i.e.,  $20^\circ$ ,  $40^\circ$ , and  $50^\circ$ ) at frequencies of 60 kHz and 200 kHz. All numerical settings were set as the same, except for the incidence angle. It can be confirmed that self-collimation can be realized over a wide range of incidence angles up to  $50^\circ$  and broadband frequencies.

## References

- [1] Colombi A, Roux P, Guenneau S, Rupin M. Directional cloaking of flexural waves in a plate with a locally resonant metamaterial. *J Acoust Soc Am* 2015;137:1783–9.
- [2] Shin YC, Yoon H, Jo S-H, Choi W, Park C-S, Kim M, et al. Phonic band gap of a quarter-wave stack for enhanced piezoelectric energy harvesting. *Int J Mech Sci* 2021;189:106003.
- [3] Jin Y, Djafari-Rouhani B, Torrent D. Gradient index phononic crystals and metamaterials. *Nanophotonics* 2019;8:685–701.
- [4] Ruiz H, Claeys C, Deckers E, Desmet W. Numerical and experimental study of the effect of microslits on the normal absorption of structural metamaterials. *Mech Syst Sig Process* 2016;70:904–18.
- [5] Cui X, Zhao J, Boyko O, Bonello B, Zhong Z. Multi-branch subwavelength focusing of the lowest-order antisymmetric Lamb mode in a gradient-index phononic crystal. *Int J Mech Sci* 2019;157:677–83.
- [6] Tol S, Degertekin F, Erturk A. Phononic crystal Luneburg lens for omnidirectional elastic wave focusing and energy harvesting. *Appl Phys Lett* 2017;111:013503.
- [7] Zhou W, Chen W, Destrade M, Lim C. Actively controllable topological phase transition in phononic beam systems. *Int J Mech Sci* 2020;105668.

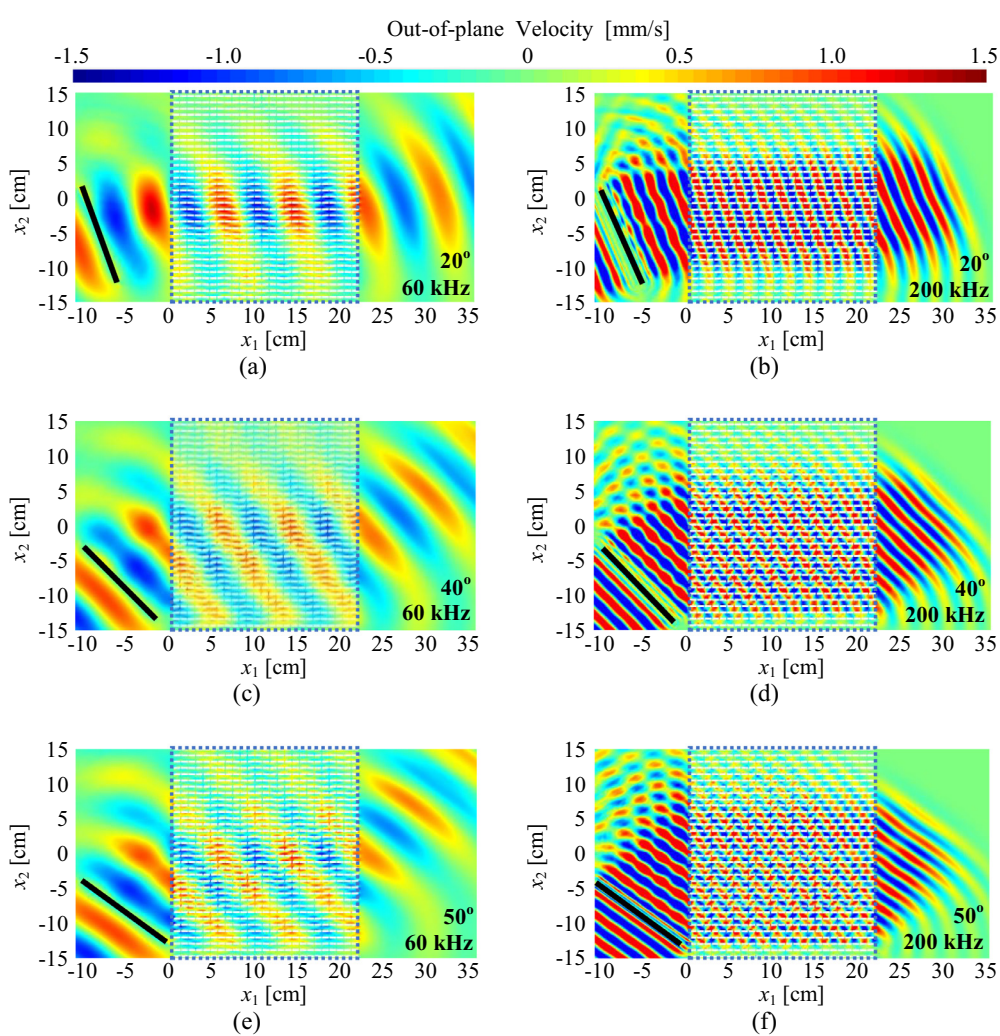


**Fig. A2.** Out-of-plane velocity fields of the structure for (a)  $20^\circ$  and 60 kHz; (b)  $20^\circ$  and 200 kHz; (c)  $40^\circ$  and 60 kHz; (d)  $40^\circ$  and 200 kHz; (e)  $50^\circ$  and 60 kHz; and (f)  $50^\circ$  and 200 kHz.

- [8] Qu J, Kadic M, Wegener M. Three-dimensional poroelastic metamaterials with extremely negative or positive effective static volume compressibility. *Extreme Mech Lett* 2018;22:165–71.
- [9] Jo S-H, Yoon H, Shin YC, Choi W, Park C-S, Kim M, et al. Designing a phononic crystal with a defect for energy localization and harvesting: supercell size and defect location. *Int J Mech Sci* 2020;179:105670.
- [10] Zhu J, Chen H, Wu B, Chen W, Balogun O. Tunable band gaps and transmission behavior of SH waves with oblique incident angle in periodic dielectric elastomer laminates. *Int J Mech Sci* 2018;146:81–90.
- [11] Han X, Zhang Z. Acoustic beam controlling in water by the design of phononic crystal. *Extreme Mech Lett* 2020;34:100602.
- [12] Korozu N, Kaya O, Cicek A, Ulug B. Self-collimation and slow-sound effect of spoof surface acoustic waves. *J Appl Phys* 2019;125:074901.
- [13] Zhao L, Lai C, Yu M. Modified structural Luneburg lens for broadband focusing and collimation. *Mech Syst Sig Process* 2020;144:106868.
- [14] Shen C, Jing Y. Loss-induced enhanced transmission in anisotropic density-near-zero acoustic metamaterials. *Sci Rep* 2016;6:37918.
- [15] Lee S-G, Kim K-J, Kim S-H, Kee C-S. Self-collimation-based photonic crystal notch filters. *J Phys D: Appl Phys* 2017;50:205102.
- [16] Lee HJ, Lee J-R, Moon SH, Je T-J, Jeon E-C, Kim K, et al. Off-centered double-slit metamaterial for elastic wave polarization anomaly. *Sci Rep* 2017;7:15378.
- [17] Yuan J, Shu J, Jiang L. Multifunctional beam steering via switchable negative refraction, self-collimation, and zero refraction effects in conventional and annular photonic crystals. *Opt Express* 2020;28:5367–77.
- [18] Auld BA. Acoustic fields and waves in solids. John Wiley & Sons; 1973.
- [19] Chigrin DN, Enoch S, Torres CMS, Tayeb G. Self-guiding in two-dimensional photonic crystals. *Opt Express* 2003;11:1203–11.
- [20] Prather DW, Shi S, Murakowski J, Schneider GJ, Sharkawy A, Chen C, et al. Self-collimation in photonic crystal structures: a new paradigm for applications and device development. *J Phys D: Appl Phys* 2007;40:2635.
- [21] Li Q-B, Li Z, Wu R-x. Bending self-collimated one-way light by using gyromagnetic photonic crystals. *Appl Phys Lett* 2015;107:241907.
- [22] Li J, Wu F, Zhong H, Yao Y, Zhang X. Acoustic beam splitting in two-dimensional photonic crystals using self-collimation effect. *J Appl Phys* 2015;118:144903.
- [23] Wen J, Yu D, Cai L, Wen X. Acoustic directional radiation operating at the pass band frequency in two-dimensional photonic crystals. *J Phys D: Appl Phys* 2009;42:115417.
- [24] Shi J, Lin S-CS, Huang TJ. Wide-band acoustic collimating by phononic crystal composites. *Appl Phys Lett* 2008;92:111901.
- [25] Liu W, Su X. Collimation and enhancement of elastic transverse waves in two-dimensional solid phononic crystals. *Phys Lett A* 2010;374:2968–71.
- [26] Park JH, Ma PS, Kim YY. Design of phononic crystals for self-collimation of elastic waves using topology optimization method. *Struct Multidisciplinary Optimiz* 2015;51:1199–209.
- [27] Chang S-Y, Chen C-D, Yeh J-Y, Chen I-W. Elastic wave propagation of two-dimensional metamaterials composed of auxetic star-shaped honeycomb structures. *Crystals* 2019;9:121.
- [28] Casadei F, Rimoli J. Anisotropy-induced broadband stress wave steering in periodic lattices. *Int J Solids Struct* 2013;50:1402–14.
- [29] Celli P, Zhang W, Gonella S. Pathway towards programmable wave anisotropy in cellular metamaterials. *Phys Rev Appl* 2018;9:014014.
- [30] Zhang H, Chen Y, Liu X, Hu G. An asymmetric elastic metamaterial model for elastic wave cloaking. *J Mech Phys Solids* 2020;135:103796.
- [31] Phani AS, Woodhouse J, Fleck N. Wave propagation in two-dimensional periodic lattices. *J Acoust Soc Am* 2006;119:1995–2005.
- [32] Kweun JM, Lee HJ, Oh JH, Seung HM, Kim YY. Transmodal Fabry-Pérot resonance: theory and realization with elastic metamaterials. *Phys Rev Lett* 2017;118:205901.
- [33] Pichard H, Torrent D. Dynamic homogenization of viscoelastic phononic metasolids. *AIP Adv* 2016;6:121705.
- [34] Ahsani S, Boukadia R, Droz C, Claeys C, Deckers E, Desmet W. Diffusion based homogenization method for 1D wave propagation. *Mech Syst Sig Process* 2020;136:106515.
- [35] Jaeken JW, Cottenier S. Solving the Christoffel equation: phase and group velocities. *Comput Phys Commun* 2016;207:445–51.
- [36] Ahn YK, Lee HJ, Kim YY. Conical refraction of elastic waves by anisotropic metamaterials and application for parallel translation of elastic waves. *Sci Rep* 2017;7:10072.
- [37] DePauw D, Al Ba'b'a H, Nouh MA. Metadamping and energy dissipation enhancement via hybrid phononic resonators. *Extreme Mech Lett* 2018;18:36–44.
- [38] Krushynska A, Miniaci M, Bosia F, Pugno N. Coupling local resonance with Bragg band gaps in single-phase mechanical metamaterials. *Extreme Mech Lett* 2017;12:30–6.
- [39] He J, Kang Z. Achieving directional propagation of elastic waves via topology optimization. *Ultrasonics* 2018;82:1–10.
- [40] Liu Y, Chang Z, Feng X-Q. Stable elastic wave band-gaps of phononic crystals with hyperelastic transformation materials. *Extreme Mech Lett* 2017;11:37–41.
- [41] Ruzzeno M, Scarpa F. Directional and band-gap behavior of periodic auxetic lattices. *Physica Status Solidi (b)* 2005;242:665–80.
- [42] Noguchi Y, Yamada T, Izui K, Nishiwaki S. Topology optimization for hyperbolic acoustic metamaterials using a high-frequency homogenization method. *Comput Meth Appl Mech Eng* 2018;335:419–71.
- [43] Lou J, Yang J, Kitipornchai S, Wu H. A dynamic homogenization model for long-wavelength wave propagation in corrugated sandwich plates. *Int J Mech Sci* 2018;149:27–37.
- [44] Zhu J, Bettaiab MB, Abed-Meraim F. Numerical investigation of necking in perforated sheets using the periodic homogenization approach. *Int J Mech Sci* 2020;166:105209.
- [45] Oh JH, Kwon YE, Lee HJ, Kim YY. Elastic metamaterials for independent realization of negativity in density and stiffness. *Sci Rep* 2016;6:23630.
- [46] Park JH, Lee HJ, Kim YY. Characterization of anisotropic acoustic metamaterial slabs. *J Appl Phys* 2016;119:034901.
- [47] Yang X, Kim YY. Topology optimization for the design of perfect mode-converting anisotropic elastic metamaterials. *Compos Struct* 2018;201:161–77.
- [48] Gréhan B. Acoustics in buildings. Thomas Telford; 1996.
- [49] Nouh M, Aldraihem O, Baz A. Wave propagation in metamaterial plates with periodic local resonances. *J Sound Vib* 2015;341:53–73.
- [50] Jo S-H, Yoon H, Shin YC, Kim M, Youn BD. Elastic wave localization and harvesting using double defect modes of a phononic crystal. *J Appl Phys* 2020;127:164901.
- [51] Gao C, Halim D, Yi X. Study of bandgap property of a bilayer membrane-type metamaterial applied on a thin plate. *Int J Mech Sci* 2020;105708.
- [52] Assis GFCA, Beli D, Miranda Jr EJP, Camino JP, Dos Santos JMC, Arruda JRF. Computing the complex wave and dynamic behavior of one-dimensional phononic systems using a state-space formulation. *Int J Mech Sci* 2019;163:105088.
- [53] Jo S-H, Yoon H, Shin YC, Youn BD. A graded phononic crystal with decoupled double defects for broadband energy localization. *Int J Mech Sci* 2020;183:105833.
- [54] Lee H, Oh JH, Seung HM, Cho SH, Kim YY. Extreme stiffness hyperbolic elastic metamaterial for total transmission subwavelength imaging. *Sci Rep* 2016;6:24026.
- [55] Sugino C, Erturk A. Analysis of multifunctional piezoelectric metastructures for low-frequency bandgap formation and energy harvesting. *J Phys D: Appl Phys* 2018;51:215103.
- [56] Zhu R, Chen Y, Wang Y, Hu G, Huang G. A single-phase elastic hyperbolic metamaterial with anisotropic mass density. *J Acoust Soc Am* 2016;139:3303–10.
- [57] D'Aguanno G, Le K, Trimm R, Alù A, Mattiucci N, Mathias A, et al. Broadband metamaterial for nonresonant matching of acoustic waves. *Sci Rep* 2012;2:340.
- [58] Kim Y-H. Sound propagation: an impedance based approach. John Wiley & Sons; 2010.
- [59] Graff KF. Wave motion in elastic solids. Ohio State University Press; 1975.